Energy-dependent photoelectron angular distributions of two-color two-photon above threshold ionization of atomic helium

Louis H. Haber, Benjamin Doughty, and Stephen R. Leone

Phys. Rev. A **84**, 013416 — Published 21 July 2011

DOI: 10.1103/PhysRevA.84.013416

Energy-dependent photoelectron angular distributions of two-color two-photon above threshold ionization of atomic helium

Louis H. Haber,* Benjamin Doughty, and Stephen R. Leone

Departments of Chemistry and Physics, and Lawrence Berkeley National Laboratory, University of California, Berkeley, CA 94720

* Present address: Department of Chemistry, Columbia University, New York, New York 10027

Energy-dependent photoelectron angular distributions from two-color two-photon above threshold ionizations are investigated to determine the partial-wave characteristics of free-free electronic transitions in helium. Sideband photoelectron energies ranging from 0.18 to 13.0 eV are measured with different wavelengths of the perturbative infrared dressing field as well as different individually-selected high-order harmonics. Using the experimentally-measured cross-section ratios and anisotropy parameters together with analytical expressions derived from second-order perturbation theory, the partial-wave branching fractions going to the *S* and *D* waves in the positive and negative sidebands are determined as a function of photoelectron kinetic energy. The results provide a sensitive test for theoretical models of two-color two-photon above threshold ionization in atoms and molecules.

PACS numbers: 32.80.Rm, 32.80.Wr, 32.80.Fb, 42.65.Ky

I. Introduction

Above threshold ionization (ATI) and high-order harmonic (HH) generation are two processes that occur when an intense, ultrashort laser pulse is focused into an atomic gas. ATI is the process whereby the atom absorbs more photons than are needed for ionization causing the photoelectron spectrum to have multiple peaks separated by the photon energy.[1] High-order harmonic generation provides extreme ultraviolet (EUV) and soft x-ray light at odd harmonics of the fundamental laser frequency with pulsewidths extending to attosecond timescales.[2,3] When an EUV high-order harmonic pulse is spatially and temporally overlapped with an intense infrared (IR) dressing field in an atomic sample, two-color two-photon above threshold ionization occurs resulting in positive and negative photoelectron sidebands corresponding to the absorption of the EUV photon along with the additional absorption or emission of the IR photon, respectively.[3]

In addition to providing temporal information on ultrashort EUV pulses, two-color two-photon above threshold ionization allows for detailed studies of free-free electronic transitions. The ATI sideband can serve as a cross-correlation signal when scanning the temporal delay between the EUV and IR pulses.[4,5] Sidebands between adjacent harmonics interfere, allowing the relative phases to be determined for the temporal reconstruction of attosecond pulse trains.[6-8] This technique also obtains atomic phase information from resonant and nonresonant two-photon ionizations.[9] By measuring the ATI sideband signal as a function of the relative angle between the linear polarizations of an EUV pulse from a free electron laser and an IR dressing field in helium, the relative contributions of the *S* and *D* partial waves are obtained for comparison to theoretical predictions.[10] Our recent measurements of photoelectron angular distributions (PADs) from two-color two-photon above threshold ionization of argon[11] and helium[12] provide similar

information on partial wave magnitudes as well as additional information on continuum phase shifts at low photoelectron energies where theoretical predictions are expected to break down.

Two theoretical descriptions for two-color two-photon above threshold ionization are the soft photon approximation[13] (SPA) and second-order perturbation theory[14] (SOPT). The SPA describes the free-free electronic transitions semi-classically using Volkov-Coulomb waves and is expected to give accurate results at high photoelectron energies in both perturbative and nonperturbative IR dressing field intensities. However, the SPA does not properly account for the partial-wave phase shifts and wave functions of the ATI sidebands, so the theory is expected to be inaccurate at low and intermediate photoelectron energies. SOPT treats the free-free electronic transitions quantum mechanically while including interferences between different partial-wave pathways of photoionization. In addition, SOPT provides a powerful analytical framework for describing two-color two-photon above threshold ionization in atoms over a wide range of energies.

In this paper, the energy-dependent photoelectron angular distributions from two-color two-photon above threshold ionization of atomic helium are measured using selected high-order harmonics in a perturbative infrared dressing field with velocity map imaging. By changing the EUV and IR photon energies, the cross-section ratios and PAD anisotropy parameters are measured for sideband photoelectron energies ranging from 0.18 to 13.0 eV. Analytical expressions derived from second-order perturbation theory are used to determine the partial-wave branching fractions going to the *S* and *D* waves in the positive and negative sidebands for each set of EUV and IR photon energies used. These experimental results provide a fundamental test for theoretical models of two-color two-photon above threshold ionization at low and intermediate energies, where the soft photon approximation is expected to be inaccurate.

II. Experimental Setup and Data Analysis

The experiments are performed using femtosecond extreme ultraviolet and infrared pulses in a pump-probe configuration with photoelectron velocity map imaging (VMI).[11,12,15,16] The ultrafast EUV pulses are produced using high-order harmonic generation in an argon jet. Either the 17th, 19th, 21st, or 23rd HH is selected and refocused to the interaction region using an EUV monochromator. The fundamental infrared pulse can be tuned between 1.53 and 1.58 eV. A portion of the infrared pulse is sent to a retroreflector on a translation stage to control the EUV-IR temporal delay before being focused to intersect with the EUV pulse at the interaction region in an effusive beam of atomic helium. The intensities of the EUV and IR pulses are estimated to be 1 x 10^4 W cm^{-2} and 5 x 10^{10} W cm^{-2}, respectively, which maintains perturbative field strengths, and the two pulses have an overall temporal cross-correlation of ~100 fs. The energies and angular distributions of the photoelectrons are measured using VMI[17] with an imaging micro-channel plate (MCP) detector in front of a charge-coupled device (CCD) camera connected to a computer for particle counting.[18] Because the EUV and IR linear polarizations are parallel, the resulting photoelectrons have angular distributions given by

$$I(\theta) = \frac{\sigma}{4\pi}[1 + \beta_2 P_2(\cos\theta) + \beta_4 P_4(\cos\theta)]$$

where θ is the angle between laser polarization vector and electron velocity vector, σ is the total cross section, and β_2 and β_4 are the anisotropy parameters associated with the second- and fourth-order Legendre polynomials, respectively.[19] The raw photoelectron images are inverted using pBASEX[20] to retrieve the anisotropy parameters and signal intensities as a function of photoelectron energy.

Several factors complicate the data analysis, necessitating the acquisition of photoelectron images under different experimental conditions. The ATI signal overlaps spatially with a much larger single photon ionization (SPI) signal on the detector. The overall ATI signal is only ~3% of the SPI signal, and there is an accompanying ~3% depletion of the SPI peak. To accurately determine the relative intensities of the positive and negative ATI sidebands as well as the PAD anisotropies of each sideband, both the EUV-only background image and the EUV+IR signal image are acquired using a computer-controlled beam block that opens and shuts on the IR pulse in synchronization with an automated file saving program. Subtraction of the EUV-only background image from the EUV+IR signal image gives positive intensities near the ATI radial peaks and negative intensities near the SPI radial peak due to depletion. However, inaccuracies result when inverting images that contain significant negative values. By subtracting a series of percentages ranging from 0 to 100% of the EUV-only background from the EUV+IR signal images, and by inverting each of these background-subtracted images separately, an accurate analysis of the ATI portion of the signal is achieved.[11,12] In addition to the ATI and SPI photoelectron signals, there is a low level of multiphoton ionization (MPI) of the background gases from the IR pulse alone. This MPI background overlaps with the negative ATI sideband of the 17^{th} high-order harmonic, obscuring the results. By switching the temporal delay stage position between t = 0 fs, corresponding to a maximum ATI signal, and t = +1 ps, corresponding to a signal composed of SPI and MPI only, the difference between the ATI signal and the MPI background is determined, allowing for MPI signal to be removed from the 17^{th} HH + IR images. All photoelectron images are recorded at ~1 minute intervals with alternating beam block and/or delay stage positions over approximately 1 day of data acquisition for each set of photon energies.

III. Results

The EUV and IR photon energies are varied to study free-free electronic transitions from two-color two-photon above threshold ionization of helium. Six different sets of EUV and IR photon energies are used to determine the energy-dependent cross-section ratios between the positive and negative ATI sidebands as well as the photoelectron angular distribution anisotropy parameters of each sideband. The first three sets of photon energies are denoted here as the low energy range, where the negative ATI sideband photoelectron energies are very close to threshold, and where the fundamental IR energy is varied over 1.55, 1.56, and 1.57 eV while the corresponding 17^{th} high-order harmonic EUV energy is varied over 26.3, 26.5, and 26.7 eV, respectively. The raw and inverted photoelectron images from the 17^{th} HH only and the 17^{th} HH in an IR dressing field at the three different fundamental IR wavelengths are shown in Figs. 1(a)-(f). The laser polarization direction is oriented vertically for all images with the polarization parallel to the detector face. Figs. 1(a), (c), and (e), which use the 17^{th} HH only, clearly exhibit single rings for SPI of helium. Figs. 1(b), (d), and (f), which show the photoelectron images using the 17^{th} HH + IR after the MPI signal from the IR pulse alone is subtracted and after 85% of the corresponding EUV-only background image is subtracted, clearly exhibit the negative (inner) and positive (outer) ATI sideband rings.

The second three sets of photon energies are denoted here as the intermediate energy range, where the EUV photon energy is varied by selecting different harmonic orders ranging from the 19^{th} to the 23^{rd} HH. The raw and inverted photoelectron images from the 19^{th} HH only, the 21^{st} HH only, and the 23^{rd} HH only are displayed in Figs. 2(a), (c), and (e), respectively,

clearly showing single rings from SPI of helium. Figs. 2(b), (d), and (f) show the photoelectron images using the 19th HH + IR, the 21st HH + IR, and the 23rd HH + IR, respectively, using 85% background subtraction of the corresponding EUV-only images. Signals near the image centers in Figs. 2(b), (d), and (e) are from multiphoton ionization of background gases from the IR pulse alone as well as electrons generated by low levels of electrical arcing from the higher voltages required on the VMI plates, which do not affect the overall results. Background subtraction percentages of 85% allow for high contrast of the ATI sideband rings while avoiding significant negative intensities on the SPI ring.

The photoelectron energy spectrum of each photoelectron image is determined from the inverted image's radial distribution, where the radius outward from the image center is proportional to the photoelectron speed. Fig. 3 shows two sets of representative photoelectron spectra. Fig. 3(a) shows the photoelectron energy spectra from the 17th HH + 794 nm and the 17th HH only, while Fig. 3(b) shows the photoelectron spectra from the 21st HH + 810 nm and the 21st HH only, where the EUV+IR spectra use 85% background subtraction. The EUV-only peaks are centered at 1.95 and 7.56 eV, respectively, as expected for single-photon ionization of ground-state helium using photon energies of 26.54 and 32.15 eV, respectively. The full-width half maxima of these two SPI peaks are 0.34 and 0.96 eV, respectively. The negative ATI sidebands in Figs. 3(a) and (b) are centered at 0.39 and 6.03 eV, respectively, with full-width half maxima of 0.27 and 0.88 eV, respectively, while the positive ATI sidebands are centered at 3.51 and 9.09 eV, respectively, with full-width half maxima of 0.45 and 1.10 eV, respectively. All photoelectron spectra, including those not shown that correspond to Figs. 1(a), (b), (e), and (f), and 2(a), (b), (e), and (f), indicate that the high-order harmonic EUV photon energies are equal to the harmonic order multiplied by the fundamental IR energy with no blueshifting.[21]

Each positive and negative ATI photoelectron peak energy is equal to the SPI peak energy plus or minus the IR photon energy, respectively, with no ponderomotive energy shifts,[1] which is expected for the pulse intensities used. The weak signal at low photoelectron energies in the EUV+IR spectrum in Fig. 3 (b) is from MPI of background gases. Photoelectron peak widths are due to the pulse bandwidths convolved with the instrumental resolution.

Analysis of the EUV+IR photoelectron spectra allows for the determination of the cross-section ratios between positive and negative ATI sidebands for each set of photon energies used. Because the positive and negative ATI sidebands occur simultaneously for the same EUV and IR photon conditions, the ratio of the integrated sideband signals is equal to the ratio of the cross sections. Each integrated sideband signal is determined by subtracting the EUV-only photoelectron spectrum from the corresponding scaled EUV+IR photoelectron spectrum at a given background subtraction percentage and integrating the resulting sideband peak over the full-width half maximum. This is done for each background percentage that is subtracted in order to obtain the conditions for accurate analysis. The cross-section ratios between the positive and negative ATI sidebands for the 17^{th} HH + 794 nm and the 21^{st} HH + 810 nm are plotted in Fig. 4 as a function of the percentage of background subtracted, which are seen to be constant at 1.12 ± 0.03 and 1.25 ± 0.04, respectively, up to a percentage of background subtracted of around 90%, where significant negative intensities in the EUV+IR image lead to inaccuracies in the inversions. This general trend is observed for all sets of photon energies investigated in this study. The cross-section ratios for each set of photon energies are plotted in Fig. 5 as a function of EUV photon energy and the values are listed in Table 1. These results are explained in more detail by analyzing the partial-wave branching fractions going to the *S* and *D* waves in the positive and negative sidebands in the discussion below.

The anisotropy parameters for the single-photon ionization PADs are first measured to test the quantitative accuracy of the VMI setup and analysis. For SPI of helium at non-relativistic photoelectron energies far from electronic excitation resonances, a single *P* wave is expected corresponding to anisotropy parameters of $\beta_2 = 2$ and $\beta_4 = 0$, resulting in a photoelectron angular distribution that is proportional to $cos^2\theta$. All experimentally measured anisotropy parameters are taken from a weighted average over the full-width half maximum of each photoelectron peak. The anisotropy parameters associated with the second-order Legendre polynomial measured for SPI of helium from the EUV-only images of Figs. 1 (a), (c), and (e), and Figs. 2 (a), (c), and (e) are $\beta_2 = 1.98 \pm 0.03$, 1.99 ± 0.03, 1.98 ± 0.04, 2.02 ± 0.03, 2.02 ± 0.04, and 2.04 ± 0.06, respectively, while the anisotropy parameters associated with the fourth-order Legendre polynomial are $\beta_4 = -0.02 \pm 0.03$, -0.02 ± 0.04, -0.02 ± 0.03, 0.01 ± 0.02, 0.01 ± 0.02, and -0.02 ± 0.04, respectively. These anisotropy parameters are all in excellent agreement with expectations for a single *P* wave, demonstrating the high accuracy of the velocity map imaging setup and data analysis.

The anisotropy parameters of the ATI sidebands are more difficult to determine because the ATI sidebands energetically overlap with the SPI peaks. This overlap causes angular averaging effects dependent on the relative intensities between the ATI sidebands and the SPI electrons over the sideband peak of interest. Changing the percentage of the EUV-only background that is subtracted from the EUV+IR images causes changes in the observed anisotropy parameters of the ATI sidebands. Using the equation, $\beta_{i,o} = R_b \beta_{i,b} + R_s \beta_{i,s}$, where $\beta_{i,o}$ is the empirically observed anisotropy parameter of the ATI peak, $\beta_{i,b}$ is the anisotropy parameter of the background at the ATI peak energy, and R_b and R_s are the relative intensities of the background and ATI signal such that $R_b + R_s = 1$, the corrected anisotropy parameter of the ATI

signal of interest, $\beta_{i,s}$, is obtained.[11,12] The observed and corrected anisotropy parameters as a function of the percentage of background subtracted for the 17th HH + 794 nm and for the 19th HH + 810 nm ATI sidebands are shown in Figs. 6 and 7, respectively. While the observed anisotropy parameters change significantly as a function of the percentage of background subtracted, the corrected anisotropy parameters are constant up to about 90% background subtraction, when negative intensities in the image cause inaccuracies in the inversion. This data analysis technique is repeated for each set of photon energies used, giving the same general trend and allowing the corrected anisotropy parameters to be determined for all positive and negative ATI sidebands. The corrected anisotropy parameters are shown in Fig. 8, plotted as a function of sideband photoelectron energy, and the values are listed in Table 1. These values are all smoothly varying as a function of photoelectron energy, with the largest changes occurring near threshold, where large variations in phase shifts and matrix elements are expected, as discussed below. Additionally, the corrected anisotropy parameters result in PAD intensities that are non-negative, to within experimental uncertainty, for all angles for each ATI sideband, satisfying the necessary condition of the measurement.[22]

IV. Discussion

The experimental results for the cross-section ratios and photoelectron angular distributions from the energy-dependent two-color two-photon above threshold ionization of helium allow for the determination of the partial-wave branching fractions going to the *S* and *D* waves in the positive and negative sidebands using second order perturbation theory. From

SOPT, the two-photon ATI sideband transition matrix elements between the initial state *i* and final state *f* are complex, given by

$$M_{if} = \langle f|D_2 \text{ pv}(E-H)^{-1}D_1|i\rangle - i\pi\langle f|D_2|k_0\rangle\langle k_0|D_1|i\rangle$$

where $D_j = \boldsymbol{F}_j \cdot \boldsymbol{r}$ is the dipole operator of the involved field F_j, pv refers to the principal value integral, H is the Hamiltonian of the unperturbed atom, and $E = E_0 + \omega_1$ is the energy of the intermediate continuum state, k_0.[14] The real part of the two-photon matrix element corresponds to a principal value integration over the continuum. The imaginary part of the two-photon matrix element is a simple product of single-photon matrix elements. The two-photon ATI sideband cross section is given by $\sigma = \sum_{if}\left|M_{if}\right|^2$, and the photoelectron angular distributions using collinear photon polarizations are given by $I(\theta,\varphi) = \sum_i \left|\sum_f M_{if}\, e^{i\delta_{l_f}} Y_{l_f m_f}(\theta,\varphi)\right|^2$, where δ_{l_f} is the phase shift of the final state partial wave of angular momentum l_f, and Y_{lm} is the spherical harmonic as a function of the inclination and azimuth angles θ and φ, respectively, with respect to the laser polarization vector.[14] Using dipole selection rules and the properties of spherical harmonics, the photoelectron angular distribution anisotropy parameters are given by

$$\beta_2 = \frac{\frac{8}{7}|(d)|^2 + 4\,Re\left[(s)(d)^* e^{i(\delta_0-\delta_2)}\right]}{|(s)|^2 + \frac{4}{5}|(d)|^2}$$

$$\beta_4 = \frac{72}{35}\left(X^2 + \frac{4}{5}\right)^{-1}$$

where (s) is the complex two photon matrix element of the *S* wave, (d) is the complex two photon matrix element of the *D* wave, and $X^2 = |(s)|^2/|(d)|^2$.[12]

In order to obtain the partial-wave branching fractions of the two-color two-photon ATI of helium, the relative *S/D* character of each sideband as well as the positive/negative ratios of the *S* and *D* waves must first be determined. The relative *S/D* character of each ATI sideband for helium is equal to the ratio of the partial cross sections of the *S* and *D* waves in each sideband, which is given by

$$\frac{\sigma_s}{\sigma_d} = \frac{5|(s)|^2}{4|(d)|^2} = \frac{18}{7\beta_4} - 1$$

when the linear polarizations of the EUV and IR photons are parallel. Using the experimentally-measured PAD anisotropy parameters associated with the fourth-order Legendre polynomial for the positive and negative ATI sidebands, $\beta_4^{(+)}$ and $\beta_4^{(-)}$, respectively, the *S/D* character of each sideband is determined, with the results plotted in Fig. 9(a) as a function of the sideband photoelectron energy. The *S/D* character of the positive sideband slowly increases from 0.67 ± 0.06 at 3.28 eV to 4.56 ± 0.75 at 13.0 eV. The *S/D* character of the negative sideband displays significant changes near threshold, decreasing from 7.49 ± 1.64 at 0.18 eV to 3.71 ± 1.65 at 0.52 eV, and then rises at higher energies to 18.2 ± 11.7 at 9.90 eV. The error bars are obtained using error propagation from the values and standard deviations of the β_4 measurements. The changes in the *S/D* character of each sideband as a function of energy reflect the changes in the complex two-photon matrix elements, (*s*) and (*d*), which describe the overlap of the radial wave functions of the *S* and *D* partial waves with the intermediate *P* wave and the ground state radial wave functions, where all continuum radial wave functions depend on energy.

The positive/negative ratio of the *S* wave is defined as $\sigma_s^{(+)}/\sigma_s^{(-)}$. Similarly, the positive/negative ratio of the *D* wave is defined as $\sigma_d^{(+)}/\sigma_d^{(-)}$. These terms describe the propensity of each partial wave to branch towards either the positive or negative sideband. The *S*

and *D* wave positive/negative ratios can also be expressed as $|(s)^{+}|^2/|(s)^{-}|^2$ and $|(d)^{+}|^2/|(d)^{-}|^2$, respectively. Rearranging the expression for the cross-section ratio using the partial-wave expansion, gives

$$\frac{\sigma^{(+)}}{\sigma^{(-)}} = \frac{\sigma_s^{(+)}}{\sigma_s^{(-)}}\left(\frac{1+\sigma_d^{(+)}/\sigma_s^{(+)}}{1+\sigma_d^{(-)}/\sigma_s^{(-)}}\right) = \frac{\sigma_d^{(+)}}{\sigma_d^{(-)}}\left(\frac{1+\sigma_s^{(+)}/\sigma_d^{(+)}}{1+\sigma_s^{(-)}/\sigma_d^{(-)}}\right),$$

where the cross-section ratios are shown to depend on the *S/D* character of each individual sideband as well as the positive/negative ratios of the *S* and *D* waves. By including the expression for the *S/D* character for each sideband, the equations for the partial-wave positive/negative ratios,

$$\frac{\sigma_s^{(+)}}{\sigma_s^{(-)}} = \frac{\sigma^{(+)}}{\sigma^{(-)}}\left(\frac{18-7\beta_4^{(+)}}{18-7\beta_4^{(-)}}\right) \quad \text{and} \quad \frac{\sigma_d^{(+)}}{\sigma_d^{(-)}} = \frac{\sigma^{(+)}}{\sigma^{(-)}}\frac{\beta_4^{(+)}}{\beta_4^{(-)}}$$

are derived. From the experimental results, the positive/negative ratios of the *S* and *D* waves are obtained for each set of photon energies, with the results plotted in Fig. 9(b). The energy-dependent *S* wave positive/negative ratios are observed to be relatively constant, changing from 0.85 ± 0.06 to 0.95 ± 0.05 as the EUV energy changes from 26.3 to 36.1 eV. However, the *D* wave positive/negative ratios change significantly, especially in the low-energy range, going from 9.49 ± 1.89 to 4.29 ± 1.51 as the EUV energy changes from 26.3 to 26.7 eV, and then stay relatively constant going to 3.80 ± 2.38 at 36.1 eV. The error bars are obtained using error propagation from the values and standard deviations of the $\sigma^{(+)}/\sigma^{(-)}$ and β_4 measurements.

The energy-dependent partial-wave branching fractions of the two-color two-photon above threshold ionization of helium are determined by combining the results from Figs. 9(a) and (b). The equations for the branching fractions going to the *S* wave in the positive sideband,

the *S* wave in the negative sideband, the *D* wave in the positive sideband, and the *D* wave in the negative sideband, are given by

$$\frac{\sigma_s^{(+)}}{\sigma_s^{(+)}+\sigma_s^{(-)}+\sigma_d^{(+)}+\sigma_d^{(-)}} = \left[1+\frac{\sigma_s^{(-)}}{\sigma_s^{(+)}}+\left(\frac{\sigma_d^{(+)}}{\sigma_s^{(+)}}\right)\left(1+\frac{\sigma_d^{(-)}}{\sigma_d^{(+)}}\right)\right]^{-1},$$

$$\frac{\sigma_s^{(-)}}{\sigma_s^{(+)}+\sigma_s^{(-)}+\sigma_d^{(+)}+\sigma_d^{(-)}} = \left[1+\frac{\sigma_s^{(+)}}{\sigma_s^{(-)}}+\left(\frac{\sigma_d^{(-)}}{\sigma_s^{(-)}}\right)\left(1+\frac{\sigma_d^{(+)}}{\sigma_d^{(-)}}\right)\right]^{-1},$$

$$\frac{\sigma_d^{(+)}}{\sigma_s^{(+)}+\sigma_s^{(-)}+\sigma_d^{(+)}+\sigma_d^{(-)}} = \left[1+\frac{\sigma_d^{(-)}}{\sigma_d^{(+)}}+\left(\frac{\sigma_s^{(+)}}{\sigma_d^{(+)}}\right)\left(1+\frac{\sigma_s^{(-)}}{\sigma_s^{(+)}}\right)\right]^{-1},$$

and

$$\frac{\sigma_d^{(-)}}{\sigma_s^{(+)}+\sigma_s^{(-)}+\sigma_d^{(+)}+\sigma_d^{(-)}} = \left[1+\frac{\sigma_d^{(+)}}{\sigma_d^{(-)}}+\left(\frac{\sigma_s^{(-)}}{\sigma_d^{(-)}}\right)\left(1+\frac{\sigma_s^{(+)}}{\sigma_s^{(-)}}\right)\right]^{-1},$$

respectively, with the results plotted in Fig. 10 as a function of EUV photon energy. The branching fractions all vary smoothly with energy. The branching fractions going to the *S* waves in the positive and negative sidebands increase with increasing EUV photon energy from 0.26 ± 0.01 and 0.31 ± 0.04, respectively, at 26.3 eV, to 0.43 ± 0.01 and 0.45 ± 0.04, respectively, at 36.1 eV. The branching fractions going to the *D* waves in the positive and negative sidebands decrease with increasing EUV photon energy from 0.39 ± 0.04 and 0.04 ± 0.01, respectively, at 26.3 eV, to 0.09 ± 0.04 and 0.02 ± 0.01, respectively, at 36.1 eV. The partial-wave branching fractions provide a comprehensive picture of the energy-dependent partial-wave characteristics of two-color two-photon ionization of helium. The ratios of the branching fractions are all consistent with the results in Figs. 9(a) and (b), and the sums of all the branching fractions are equal to one for all photon energies, as expected.

If the photon energies are increased further to a high energy regime, such that the photoelectron energies of the sidebands are at least 15 times greater than the IR dressing field photon energy, the soft-photon approximation[13] would be expected to be accurate. This would correspond to sideband photoelectron energies that are greater than 23 eV and EUV photon energies that are greater than 49 eV for ATI measurements from helium using 800 nm dressing fields. The soft-photon approximation gives theoretically predicted anisotropy parameters of β_2 = 2.86 and β_4 = 1.14 for both the positive and negative ATI sidebands of helium, and a cross-section ratio that asymptotically approaches 1.00.[12] This yields a predicted *S/D* character of 1.25 for each sideband, a predicted positive/negative ratio of 1.00 for both the *S* and *D* waves, and branching fractions of 0.28 and 0.22 going to the *S* and *D* waves, respectively, in both the positive and negative sidebands. However, at the energies used in this paper, the soft photon approximation is not valid because the continuum electrons cannot be accurately described as Volkov-Coulomb waves, but rather the radial wave functions of each partial wave must be solved quantum mechanically from the Hamiltonian to be used in second-order perturbation theory. Unfortunately, theoretical predictions of the energy-dependent two-photon matrix elements from helium using second-order perturbation theory are not currently available.

The experimental results for the cross-section ratios and photoelectron angular distributions from the energy-dependent two-color two-photon above threshold ionization of helium provide a fundamental test for theoretical descriptions of free-free electronic transitions. The cross-section ratios and the β_4 values provide information on the *S* and *D* partial-wave magnitudes. The β_2 values contain additional information on the real and imaginary components of the two-photon matrix elements, as well as phase shift differences between the continuum *S* and *D* partial waves. Second-order perturbation theory is expected to be accurate for the two-

color two-photon above threshold ionization of helium at low and intermediate photon energies because electron-electron correlation is small and because all initial, intermediate, and final states can be described by separable radial and angular wave functions. An accurate SOPT treatment should also include electron spin since it affects the phase shifts and radial wave functions of the continuum waves.[23] Two-color two-photon above threshold ionization from larger atoms may have additional theoretical complications due to an increased number of photoionization partial-wave pathways of higher angular momenta, electron-electron correlations, and potential breakdowns in second-order perturbation theory.

V. Conclusion

In conclusion, the energy-dependent photoelectron angular distributions and cross-section ratios of two-color two-photon above threshold ionization are measured using velocity map imaging. By changing the perturbative infrared dressing field energies as well as the individually-selected high-order harmonic extreme ultraviolet energies, the measured negative sideband photoelectron energy ranges from 0.18 to 9.90 eV while the measured positive sideband photoelectron energy ranges from 3.28 to 13.0 eV. Using the experimental results with analytical expressions derived from second order perturbation theory, the energy-dependent partial-wave branching fractions going to the *S* and *D* waves in the positive and negative sidebands are obtained, where all values vary smoothly with energy. The branching fractions going to the *S* waves in the positive and negative sidebands increase with increasing photon energies and have similar values. The branching fractions going to the *D* waves in the positive and negative sidebands decrease with increasing photon energies, with a strong preference

toward the positive sideband. These results provide a sensitive test for future theoretical models of two-color two-photon above threshold ionization in atoms.

Acknowledgments

The authors gratefully acknowledge Daniel Strasser for many helpful discussions. Financial support is provided by the Director, Office of Science, Office of Basic Energy Sciences, Chemical Sciences, Geosciences, and Biosciences Division, U.S. Department of Energy under contract No. DE-AC02-05CH11231.

References

(1) W. Becker, F. Grasbon, K. Kopold, D. B. Milosˇevic´, G. G. Pauling, and H. Walther, *Adv. At. Mol. Opt. Phys.* **48**, 35 (2002).

(2) T. Brabec and F. Krausz, *Rev. Mod. Phys.* **72**, 545 (2000).

(3) P. Agostini and L. F. DiMauro, *Rep. Prog. Phys.* **67**, 813 (2004).

(4) J. M. Schins, P. Breger, P. Agostini, R. C. Constantinescu, H. G. Muller, G. Grillon, A. Antonetti, and A. Mysyrowicz, *Phys. Rev. Lett.* **73**, 2180 (1994).

(5) M. Meyer, D. Cubaynes, P. O'Keefe, H. Luna, P. Yeats, E. T. Kennedy, J. T. Costello, P. Orr, R. Taieb, A. Maquet, S. Dusterer, P. Radcliffe, H. Redlin, A. Azima, E. Plonjes, and J. Feldhaus, *Phys. Rev. A* **74**, 011401 (2006).

(6) P. M. Paul, E. S. Toma, P. Breger, G. Mullot, F. Auge, P. Balcou, H. G. Muller, and P. Agostini, *Science* **292**, 1689 (2001).

(7) S. A. Aseyev, Y. Ni, L. J. Frasinski, H. G. Muller, and M. J. J. Vrakking, *Phys. Rev. Lett.* **91**, 223902 (2003).

(8) Y. Mairesse and. F. Quere, *Phys. Rev. A* **71**, 011401 (2005).

(9) M. Swoboda, T. Fordell, K. Klunder, J. M. Dahlstrom, M. Miranda, C. Buth, K. J. Schafer, J. Mauritsson, A. L'Huillier, and M. Gisselbrecht, *Phys. Rev. Lett.* **104**, 103003 (2010).

(10) M. Meyer, D. Cubaynes, D. Glijer, J. Dardis, P. Hayden, P. Hough, V. Richardson, E. T. Kennedy, J. T. Costello, P. Radcliffe, S. Düsterer, A. Azima, W. B. Li, H. Redlin, J. Feldhaus, R. Taïeb, A. Maquet, A. N. Grum-Grzhimailo, E. V. Gryzlova, and S. I. Strakhova, *Phys. Rev. Lett.* **101**, 193002 (2008).

(11) L. H. Haber, B. Doughty, and S. R. Leone, *J. Phys. Chem. A* **113**, 13152 (2009).

(12) L. H. Haber, B. Doughty, and S. R. Leone, *Mol. Phys.* **108**, 1241 (2010).

(13) A. Maquet and R. Taïeb, *J. Mod. Opt.* **54**, 1847 (2007).

(14) E. S. Toma and H. G. Muller, *J. Phys. B* **35**, 3435 (2002).

(15) L. H. Haber, B. Doughty, and S. R. Leone, *Phys Rev. A* **79**, 031401 (2009).

(16) B. Doughty, L. H. Haber, C. Hackett, and S. R. Leone, *J. Chem. Phys.* **(submitted)**, (2010).

(17) A. T. J. B. Eppink and D. H. Parker, *Rev. Sci. Instrum.* **68**, 3477 (1997).

(18) W. Li, S. D. Chambreau, S. A. Lahankar, and A. G. Suits, *Rev. Sci. Instrum.* **76**, 063106 (2005).

(19) K. L. Reid, *Annu. Rev. Phys. Chem.* **54**, 397 (2003).

(20) G. A. Garcia, L. Nahon, and I. Powis, *Rev. Sci. Instrum.* **75**, 4989 (2004).

(21) Z.-H. Loh, M. Khalil, R. E. Correa, and S. R. Leone, *Rev. Sci. Instrum.* **79**, 073101 (2008).

(22) C. Blondel and C. Delsart, *Laser Physics* **3**, 699 (1993).

(23) T. N. Chang and T. K. Fang, *Phys. Rev. A* **52**, 2638 (1995).

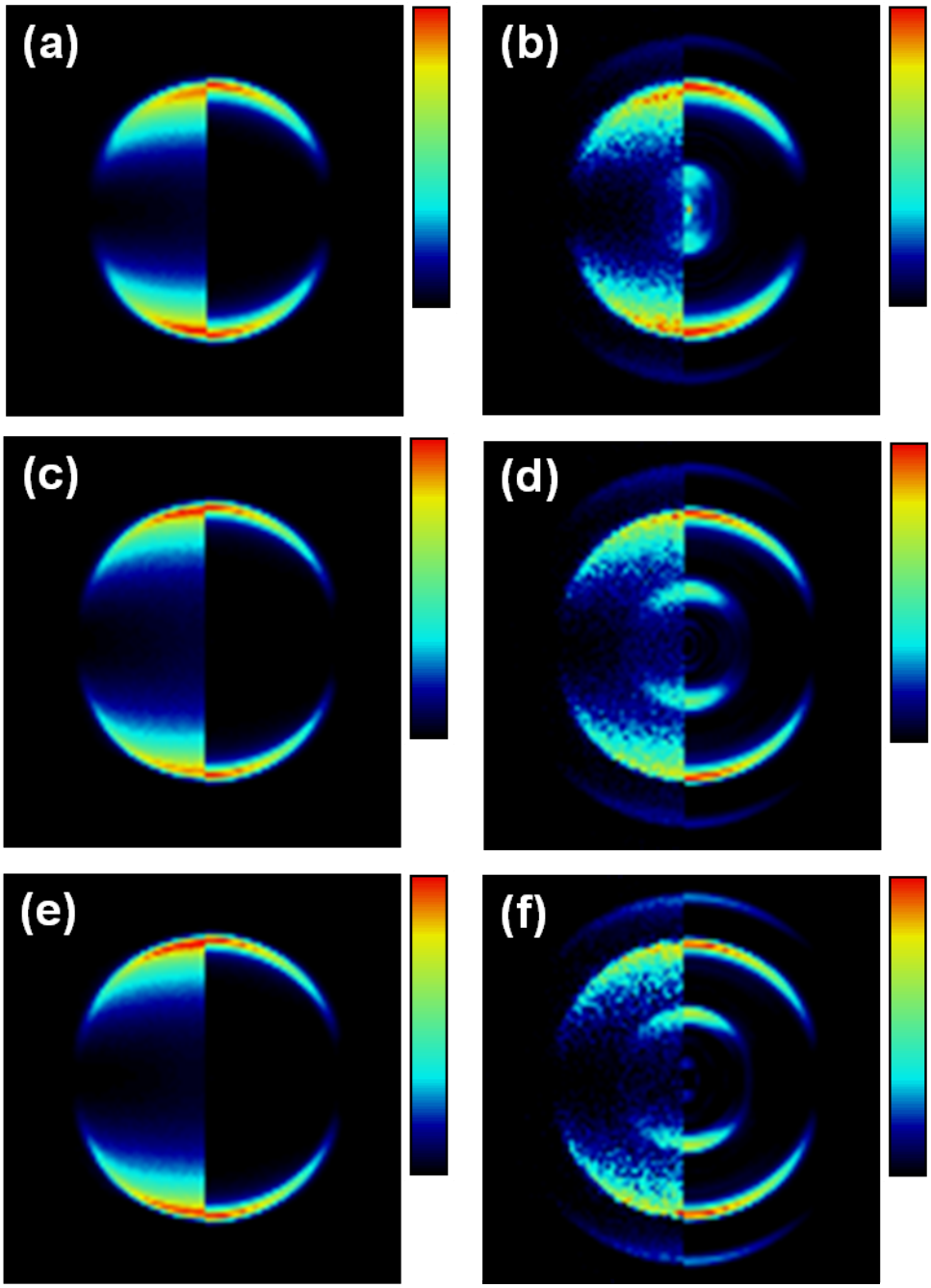

Fig. 1: Raw (left side halves) and inverted (right side halves) photoelectron images from helium using (a) the 17th HH (26.3 eV) only, (b) the 17th HH (26.3 eV) + 801 nm, (c) the 17th HH (26.5 eV) only, (d) the 17th HH (26.5 eV) + 794 nm, (e) the 17th HH (26.7 eV) only, and (e) the 17th HH (26.7 eV) + 790 nm. The laser polarization direction is oriented vertically for all images.

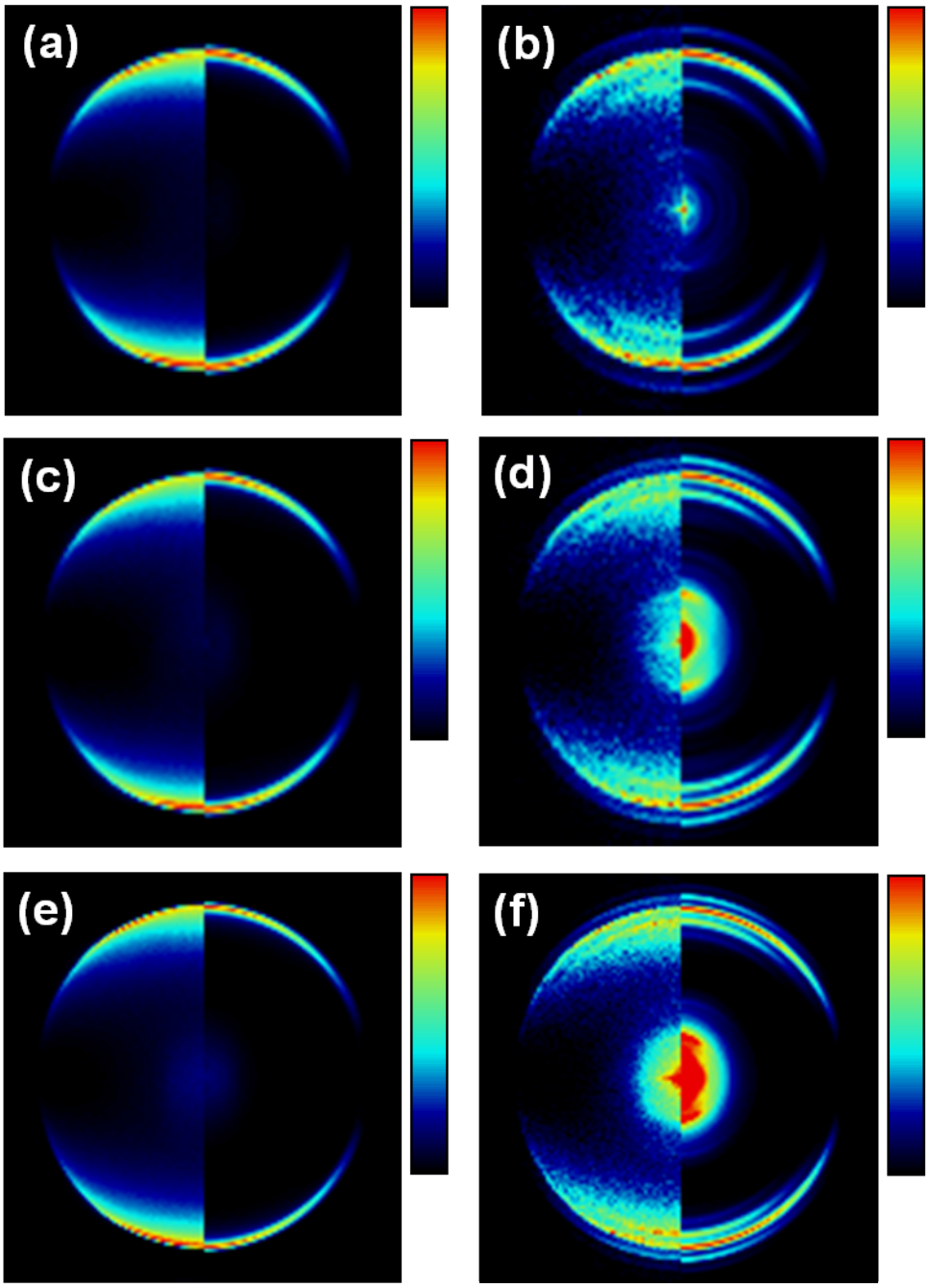

Fig. 2: Raw (left side halves) and inverted (right side halves) photoelectron images from helium using (a) the 19th HH only, (b) the 19th HH + IR, (c) the 21st HH only, (d) the 21st HH + IR, (e) the 23rd HH only, and (f) the 23rd HH + IR.

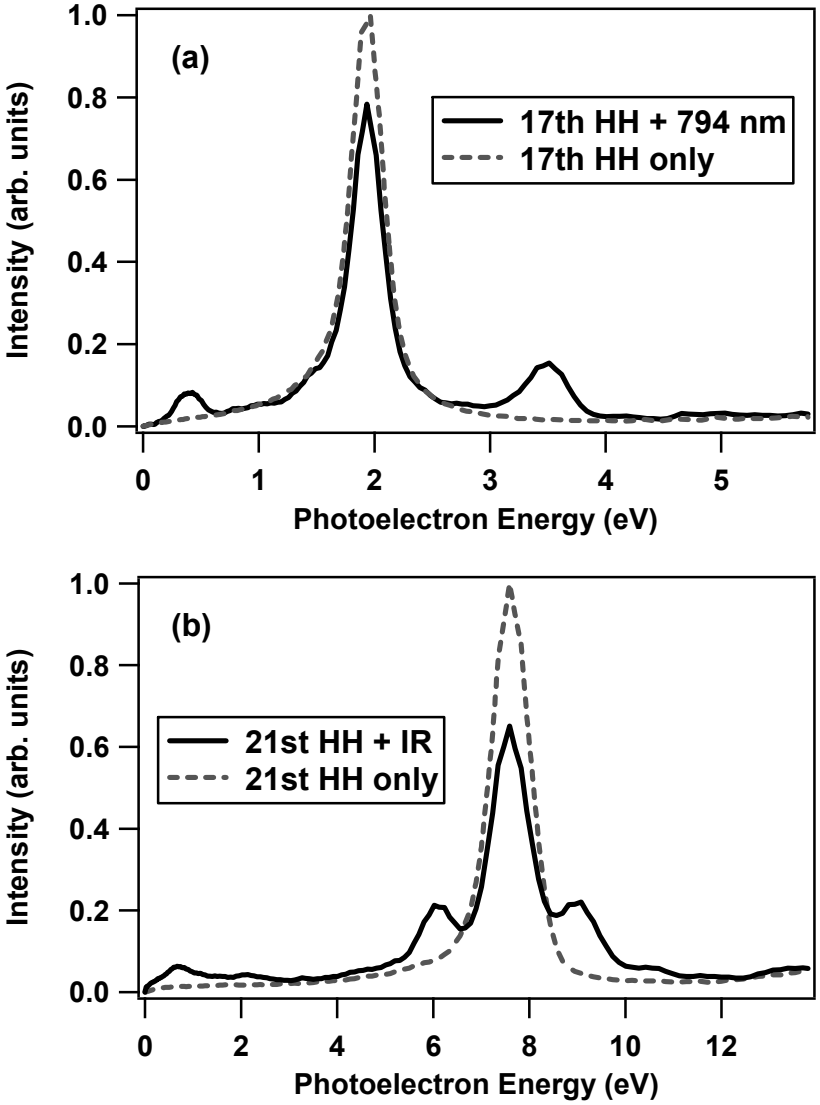

Fig. 3: Photoelectron energy spectra from helium using (a) the 17th HH + 794 nm and the 17th HH only, and (b) the 21st HH + 810 nm and the 21st HH only. These representative spectra show the positive and negative ATI sidebands as well as the SPI depletion.

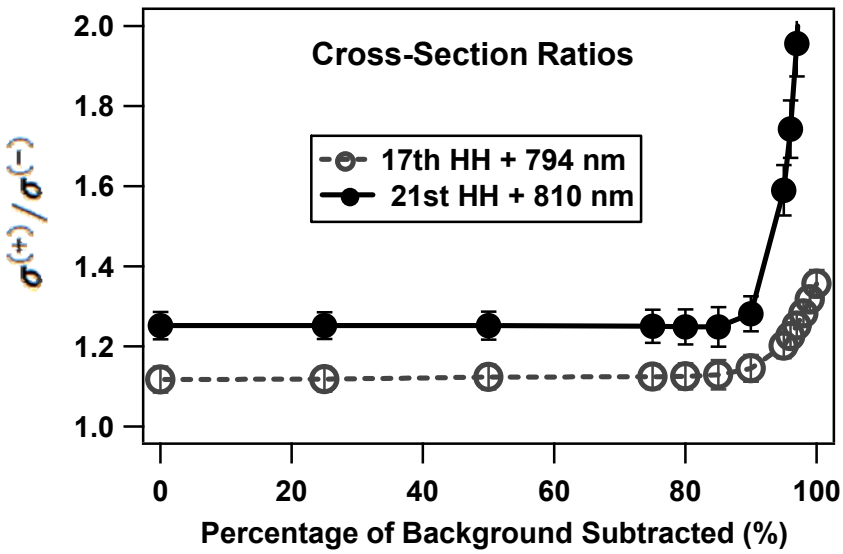

Fig. 4: The ratios of the cross sections between the positive and negative ATI sidebands for the 17^{th} HH + 794 nm and the 21^{st} HH + 810 nm as a function of the percentage of background subtracted.

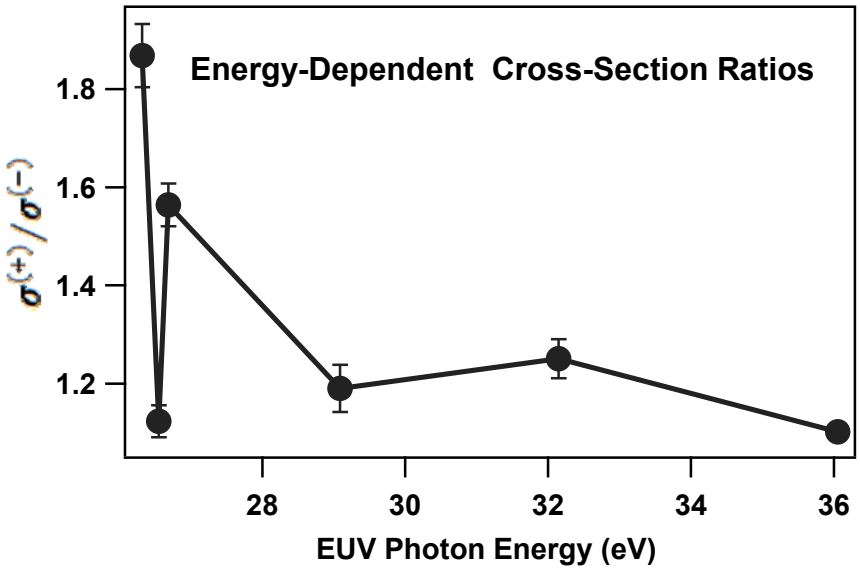

Fig. 5: Cross-section ratios between the positive and negative ATI sidebands from helium using different photon energies.

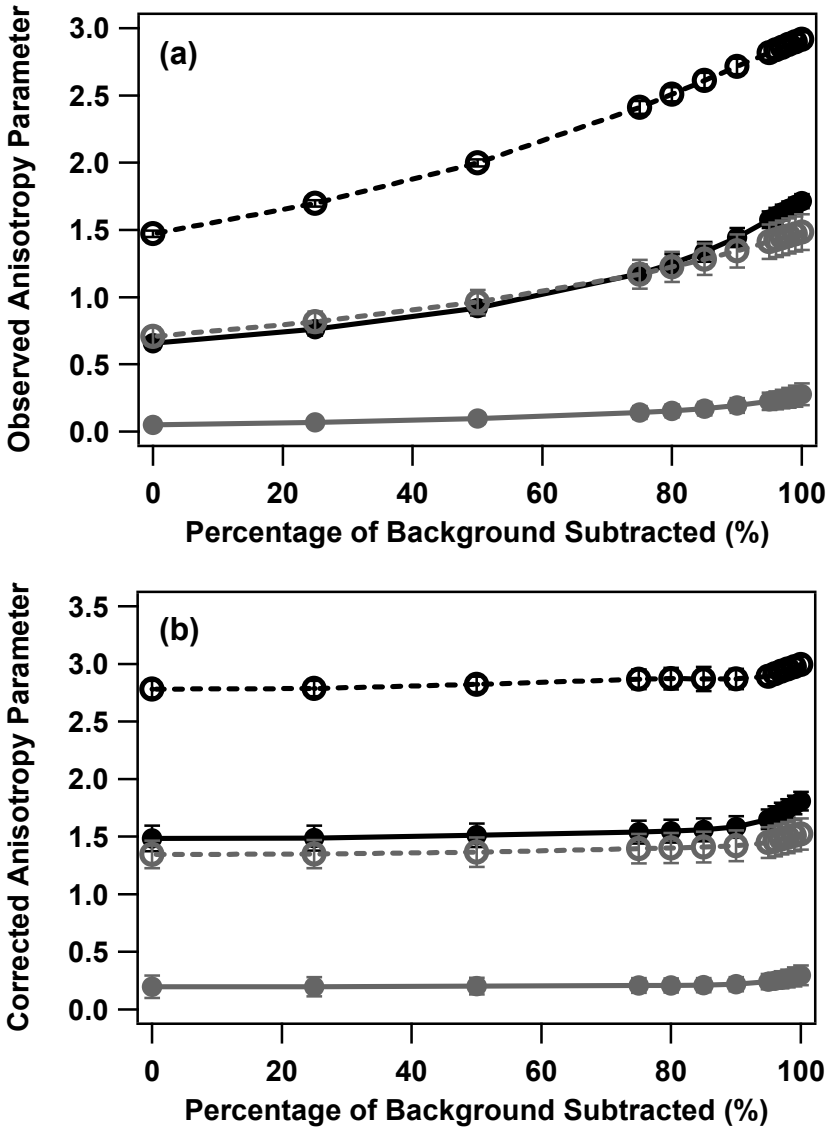

Fig. 6: (a) The observed anisotropy parameters and (b) the corrected anisotropy parameters of $\beta_2^{(-)}$ (closed black circles), $\beta_4^{(-)}$ (closed gray cirlces), $\beta_2^{(+)}$ (open black circles), and $\beta_4^{(+)}$ (open gray circles) as a function of the percentage of background subtracted for the 17th HH + 794 nm.

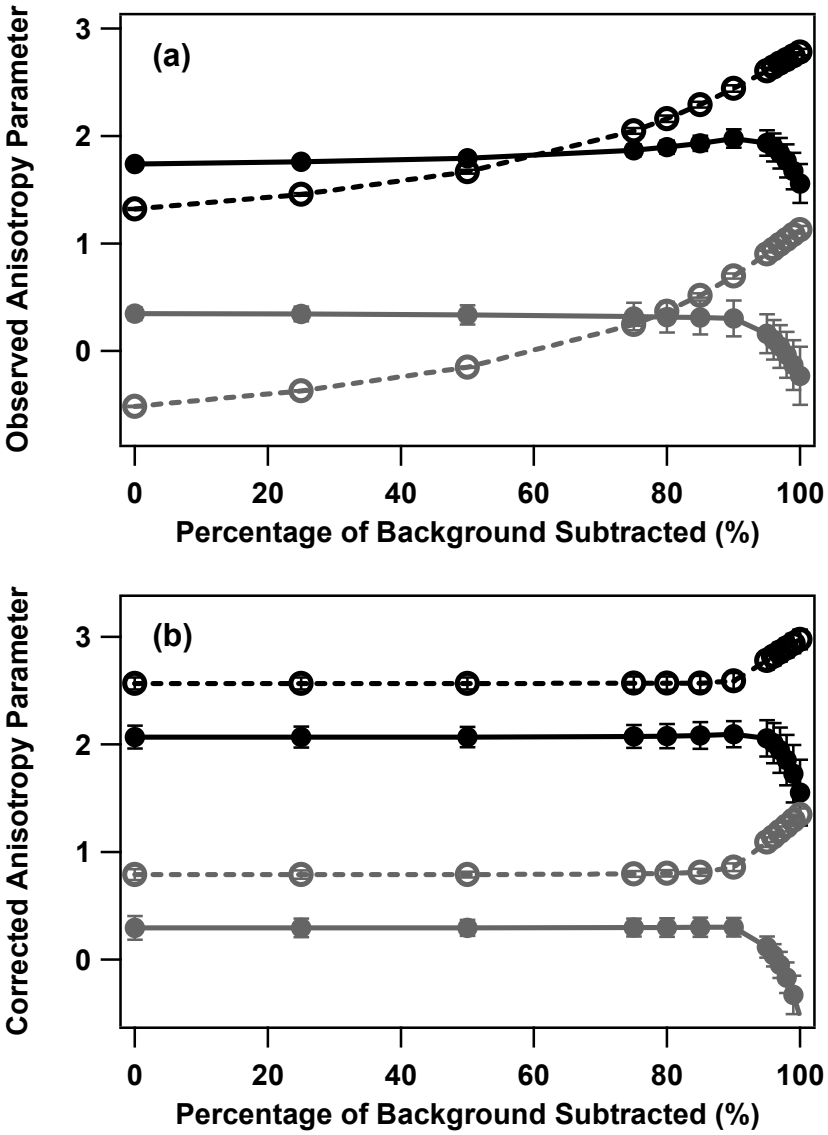

Fig. 7: (a) The observed anisotropy parameters and (b) the corrected anisotropy parameters of $\beta_2^{(-)}$ (closed black circles), $\beta_4^{(-)}$ (closed gray cirlces), $\beta_2^{(+)}$ (open black circles), and $\beta_4^{(+)}$ (open gray circles) as a function of the percentage of background subtracted for the 21st HH + 810 nm.

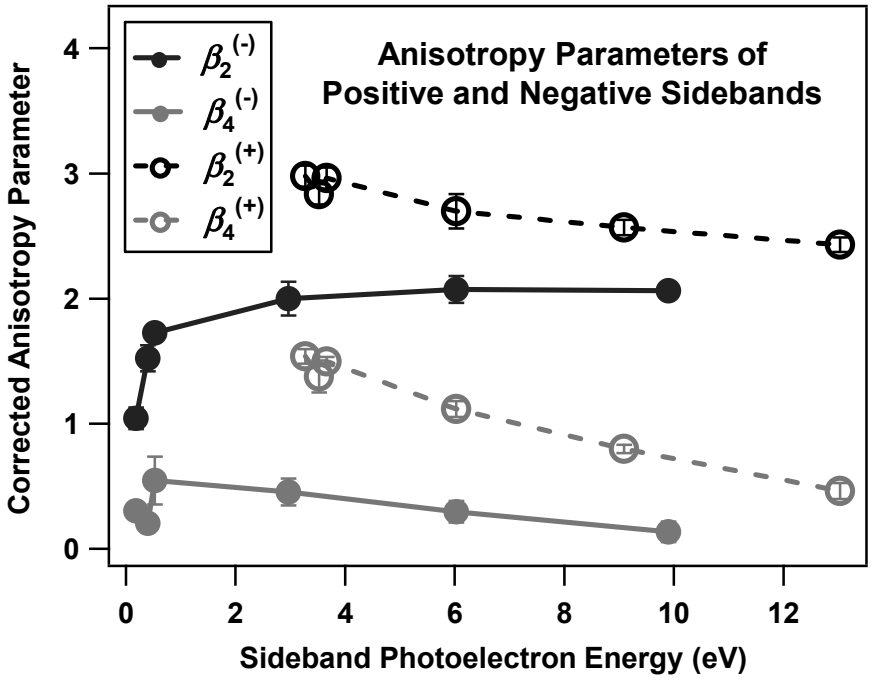

Fig. 8: Corrected anisotropy parameters of the positive and negative ATI sidebands as a function of sideband photoelectron energy.

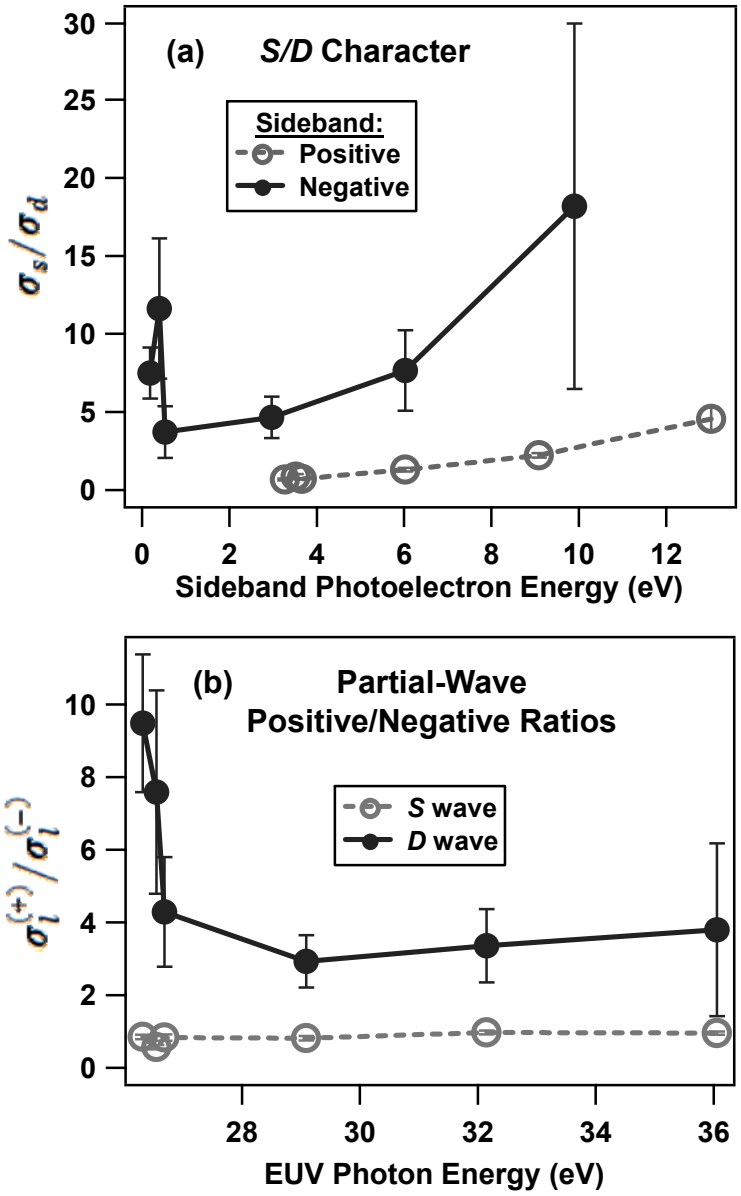

Fig. 9: (a) *S/D* character of the positive and negative ATI sidebands as a function of sideband photoelectron energy. (b) Positive/negative ratios of the *S* and *D* waves at different EUV photon energies.

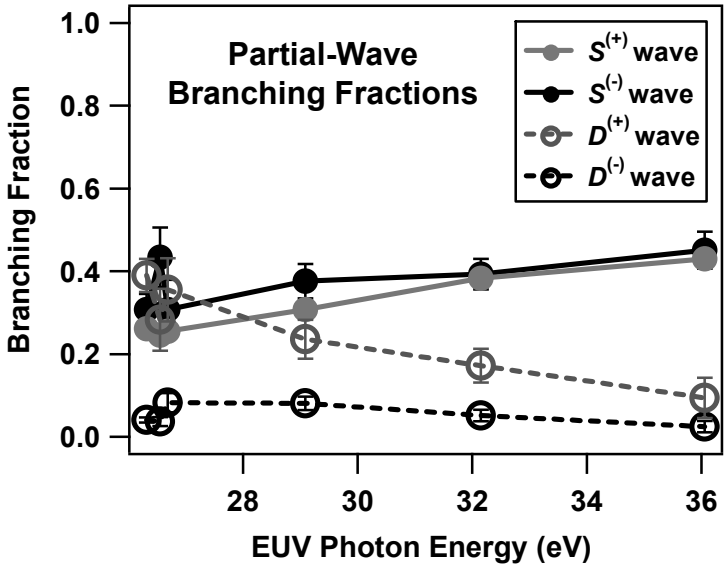

Fig. 10: Partial-wave branching fractions going to the positive sideband *S* wave (closed gray circles), the negative sideband *S* wave (closed black circles), the positive sideband *D* wave (open gray circles), and the negative sideband *D* wave (open black circles) at different EUV photon energies.

Table 1: Experimental results for positive and negative ATI sidebands from helium using different EUV and IR energies (in eV).

EUV Energy	**IR Energy**	$\boldsymbol{\sigma^{(+)}/\sigma^{(-)}}$	$\boldsymbol{\beta_2^{(-)}}$	$\boldsymbol{\beta_4^{(-)}}$	$\boldsymbol{\beta_2^{(+)}}$	$\boldsymbol{\beta_4^{(+)}}$
26.32	1.55	1.87 ± 0.06	1.04 ± 0.09	0.30 ± 0.06	2.98 ± 0.08	1.54 ± 0.06
26.54	1.56	1.12 ± 0.03	1.52 ± 0.10	0.20 ± 0.07	2.83 ± 0.08	1.38 ± 0.13
26.68	1.57	1.56 ± 0.04	1.73 ± 0.07	0.55 ± 0.19	2.96 ± 0.08	1.50 ± 0.03
29.09	1.53	1.19 ± 0.05	2.00 ± 0.14	0.45 ± 0.11	2.70 ± 0.14	1.12 ± 0.06
32.15	1.53	1.25 ± 0.04	2.07 ± 0.11	0.30 ± 0.09	2.57 ± 0.06	0.80 ± 0.03
36.06	1.57	1.10 ± 0.02	2.06 ± 0.05	0.13 ± 0.08	2.43 ± 0.06	0.46 ± 0.06